Acta Materialia 276 (2024) 120113

Contents lists available at ScienceDirect

Acta Materialia

journal homepage: www.elsevier.com/locate/actamat

A new approach for *in situ* electrochemical nanoindentation: Side charging as a promising alternative

Stefan Zeiler [a,*], Anna Sophie Jelinek [a], Velislava Terziyska [a], Ruth Schwaiger [b], Christian Mitterer [a], Steffen Brinckmann [b], Verena Maier-Kiener [a,*]

[a] *Department of Materials Science, Montanuniversität Leoben, Leoben 8700, Austria*
[b] *Microstructure and Properties of Materials (IEK-2), Forschungszentrum Jülich, Jülich 52425, Germany*

ARTICLE INFO

Keywords:
Electrochemical nanoindentation
Hydrogen charging
Hydrogen embrittlement
Ferritic steel
Diffusion
X-ray diffraction

ABSTRACT

Understanding hydrogen embrittlement in metals is an essential task for the energy transition, where hydrogen plays a key role. Besides the economic consequences of embrittlement, safety aspects are a very important factor to consider. Therefore, materials need to be screened in order to evaluate their mechanical response under hydrogen influence. Besides macroscopic mechanical testing, in situ electrochemical nanoindentation and micromechanical testing —in general— represent promising methods as they allow to characterize individual microstructural features. In the established “front-side” charging approach, hydrogen enters the sample at the same surface on which indentation tests are performed. An alternative is “back-side” charging, where hydrogen is introduced at the opposite side of the indentation location. In the present study, a novel “side” charging cell was designed and the results were compared to those obtained by “front-side” charging. For this purpose, a ferritic steel with high chromium content (X6Cr17) underwent a grain coarsening heat treatment to ensure that multiple nanoindentation experiments can be performed within a single grain. A similar grain orientation was tested with both charging approaches. The novel “side” charging cell design outperforms the stiffness of the reference front-side charging cell by 60 %. Both cell designs yielded constant Young’s moduli before, during and several hours after charging. The hardness increased during charging due to hydrogen uptake, whereas the hardness settled several hours after charging to the values before charging started. The presence of hydrogen at the indentation side was confirmed by in situ X-ray diffraction using a self-reporting titanium film.

1. Introduction

With its high gravimetric energy density of ≈ 120 MJ/kg [1], hydrogen is an essential part in the ongoing energy transition aiming to reduce carbon emissions and to stay below the 1.5 °C global warming goal defined by the Paris Agreement under the United Nations Framework Convention on Climate Change [2]. However, the use of hydrogen can cause material interactions, which lead to embrittlement and degradation in iron based alloys [3–5], nickel based alloys [6–8] and other metals, such as Ti, Cu and Al [9–11]. These detrimental effects need to be considered in related applications e.g., nuclear power, fuel cell technology and oil and gas industry [12]. Hydrogen can be introduced into a material of interest via cathodic charging, as well as high pressure hydrogen charging [13]. Another promising method to introduce hydrogen into the material and evaluate the mechanical properties is hydrogen plasma charging [14,15]. Many authors have focused on the macromechanical behavior and performed slow strain-rate tensile tests after electrolytic pre-charging [5,16]. In situ electrochemical nanoindentation (ECNI) [4,6,7,11,17] as well as in situ micromechanical testing of tensile samples, cantilevers and micro-pillars [14,18–21] have become versatile tools to investigate the mechanical response during hydrogen charging. The first reported charging cell by Barnoush et al. works with “front-side” charging approach, in which hydrogen diffuses directly into the sample at the site of indentation [22–25,11,17]. An alternative to this method is the so-called “back-side” charging reported in [3,4,6,10]. There, hydrogen diffuses into the sample from the side opposite to the nanoindentation tests. Kim et al. used this approach to design a cell which can be operated in a scanning electron microscope (SEM), enabling simultaneous testing and observation of the surface [10]. The presence of hydrogen on the tested surface was confirmed via a silver decoration method, where silver ions react with hydrogen atoms in the sample and form nanoparticles on the surface when hydrogen is

---

* Corresponding authors.
E-mail addresses: stefan.zeiler@unileoben.ac.at (S. Zeiler), verena.maier-kiener@unileoben.ac.at (V. Maier-Kiener).

https://doi.org/10.1016/j.actamat.2024.120113
Received 15 February 2024; Received in revised form 21 May 2024; Accepted 14 June 2024
Available online 14 June 2024
1359-6454/© 2024 The Authors. Published by Elsevier Ltd on behalf of Acta Materialia Inc. This is an open access article under the CC BY license (http://creativecommons.org/licenses/by/4.0/).

present [10,26]. Similar charging experiments on Ti-6Al-4V showed titanium hydride formation detected via electron backscatter diffraction (EBSD) [10]. Pogrielz et al. recently performed in situ synchrotron experiments on a duplex steel and observed an expansion of the austenitic lattice due to hydrogen charging, while the ferrite phase remained unchanged [27]. Depending on the metals tested, both approaches, front-side and back-side charging, involve advantages and disadvantages. Face centered cubic (fcc) alloys typically exhibit low diffusion coefficients, because of their higher packing density and therefore diffusion paths should be short to avoid long charging times [28]. For these metals, front-side charging provides advantages, because hydrogen uptake occurs directly at the site where the indents are performed. However, the direct contact of the tested surface with the electrolyte might lead to corrosion and makes it difficult to clearly distinguish between corrosion and hydrogen uptake effects [4]. Surface preserving electrolytes are a way to reduce corrosion damage [19]. Back-side charging avoids the contact of the tested surface with the electrolyte and corrosion effects can be excluded. However, possible hydrogen bubble formation and bursting at the interface between sample and electrolyte needs to be taken into account to avoid instabilities of the current flow and the mechanical setup. Duarte et al. and Roa et al. used Agar to form a hydrogel to ensure electrolyte-sample contact during the whole experimental procedure and to introduce more viscosity to reduce the effect of the bubble bursting [3,4]. Müller et al. continuously pumped the electrolyte through the cell to avoid bubble formation [6]. Furthermore, when using thicker samples ($>$ 2 mm), reasonable experimental times are only possible, when investigating body centered cubic (bcc) alloys with the characteristic higher diffusion constant [3,4]. When investigating fcc alloys, the sample thickness needs to be drastically reduced due to the low diffusivity, which might lead to sample bending and an overall lower system/frame stiffness [6]. Consequently, the indentation depth also needs to be reduced to minimize the applied forces. Hence, neither front-side nor back-side charging is without drawbacks and novel cell-designs might find better solutions.

In general, investigations of the small-scale mechanical response make it possible to evaluate the effects of hydrogen on the dislocation emission and dislocation mobility. Barnoush et al. investigated single crystalline Ni [22,23] and FeAl [25] as well as coarse grained Al [24] and observed decreasing pop-in loads during hydrogen charging. The same behavior was observed by Duarte et al. [4] for FeCr alloys. This reduction has been attributed to a reduction of the dislocation line energy due to interaction with the diffusible hydrogen [29]. For single crystalline Cu [23] no changes of the pop-in loads were observed. Ebner et al. reported an increased scattering of the pop-in load for a nickel based alloy due to surface steps that were produced during hydrogen charging [7]. Another observation is the hardness increase after hydrogen exposure, which is assumed to originate from Cottrell like hydrogen atmospheres close to dislocation cores, which decrease the dislocation mobility by pinning effects [3,4,7]. A decrease of the hardness and Young's modulus during front-side charging is partly explained by surface damage due to the electrolyte [4], while others explain a increasing Young's modulus by artificial phenomena like a surface pile-up formation [7].

Besides ECNI, Deng et al. performed micromechanical tests on microcantilevers inside an environmental SEM (ESEM) [20,21]. They investigated the crack growth behavior of FeAl samples in high vacuum and under water vapor pressures. The water vapor reacts with Al, which introduces hydrogen into the sample. This limits the applicability of the method to Al-containing materials. Hajilou et al. used a method similar to the aforementioned front-side charging approach to electrochemically charge and test Fe-3wt%Si micro-cantilevers [18] and micro-pillars [19]. They used a glycerol based electrolyte to avoid local corrosion. Wan et al. performed in situ slow strain-rate tensile tests and charged the sample via a hydrogen plasma in an ESEM [14]. The plasma prohibits to simultaneously image and charge the sample. Via a separate plasma charging cell inside a SEM, Massone et al. accomplished to perform tensile tests with simultaneous observation during charging [15]. Fang et al. [30] used deuterium charging with a plasma to introduce the hydrogen-isotope into tungsten and reported an increase in hardening after charging.

The current work introduces a novel cell design for ECNI and micromechanical testing, where the goal was to increase the overall system stiffness and avoid the direct contact between electrolyte and the tested sample surface by charging the sample from the side. X-ray diffraction (XRD) measurements on a sample, coated with a self-reporting Ti detection film, confirm the presence of hydrogen at the indentation side due to titanium hydride formation. The results obtained are compared with the front-side charging approach by testing the ferritic steel X6Cr17.

2. Experimental methods

2.1. Material and testing methods

Experiments were performed with the commercially available ferritic steel X6Cr17 *(Stahlog GmbH, Germany)*, which was delivered as sheet material with a thickness of 2 mm. Samples with a size of 18 mm × 18 mm for the front-side charging and 16 mm × 10 mm for the side charging and in situ XRD measurements were prepared. To increase the average grain size and enable multiple measurements within a single grain, the steel was heat treated in a vacuum furnace *(HTM Reetz GmbH, Germany)*. The temperature was increased to 1300 °C with a rate of 20 K/min and then held for 4 h to promote diffusion and grain growth. Afterwards, the temperature was decreased to 800 °C with a rate of 60 K/min and then held for 1 h resulting in an increased grain size after the cooling process with 60 K/min. After heat treatment, the samples were ground sequentially to 4000 grid SiC paper followed by a polishing with 3 μm and 1 μm diamond suspensions. In analogy to [3] the samples were etched with V2A agent for ≈ 10 s and vibropolished in a *VibroMet 2 (Buehler, USA)* with *Struers OP-U solution (Struers GmbH, Germany)* for 4 h. The side charging and in situ XRD sample was additionally wet ground to at least 4000 grid SiC paper at those surfaces, which would be in contact with the electrolyte (see Section 2.3). The aim was to produce a smooth electrolyte-sample interface, which enhances adsorption of hydrogen by reducing the recombination to gaseous hydrogen [9].

The microstructural investigations were performed in a *Tescan Clara SEM (Tescan Group, Czech Republic)* with an *Oxford Instruments Symmetry S3 Electron Back-scatter Diffraction (EBSD) detector (Oxford Instruments, United Kingdom)*. An acceleration voltage of 20 kV was used and the step size in the EBSD maps was set to 4 μm. The topography and pile-ups were measured with a *Keyence VK-X1100 laser confocal microscope (Keyence Corporation, Japan)*.

The in situ XRD sample with the aforementioned side charging geometry was additionally coated with a Ti film on its upper surface, which is jutting out from the electrolyte (see Fig. 2a). The deposition was carried out using non-reactive unbalanced magnetron sputtering in a laboratory scale deposition system. For film synthesis, a single 99.7 % purity Ti target with a diameter of 50.8 mm and a thickness of 6 mm was used. The substrate was mounted on a rotating sample holder with a distance of ≈ 45 mm to the target. The rotation speed of the sample holder was 50 rpm. The vacuum chamber was evacuated to a base pressure of $9 \cdot 10^{-6}$ mbar. Prior to deposition, substrate etching was performed for 2 min in Ar atmosphere at $3.8 \cdot 10^{-2}$ mbar, using asymmetric bipolar pulsed d.c. bias voltage of −500 V, with a frequency of 50 kHz. Simultaneously, the Ti target was sputter-cleaned, running at 0.1 A, below closed shutter. The deposition was performed in current-controlled mode for 30 min. The target current was set to 0.35 A and the Ar flow rate to 30 sccm, corresponding to $0.5 \cdot 10^{-3}$ mbar working pressure. No substrate heating was applied. The resulting film thickness was ≈ 500 nm.

2.2. Indentation

All indentation experiments and the corresponding in situ designs were implemented in a *KLA G200 nanoindenter (KLA, USA)*. Experiments were performed at room temperature with a diamond Berkovich tip *(Synton-MDP, Switzerland)* and a constant indentation strain-rate ($\dot{P}/P$) of 0.05 s^{-1} up to an indentation depth of 2000 nm. The tip movement was superimposed with a harmonic displacement of 2 nm and a frequency of 45 Hz, which allows a continuous stiffness measurement (CSM) and therefore a continuous evaluation of Young's modulus and hardness. All experiments were evaluated according to Oliver and Pharr [31] using a Poisson's ratio of 0.29 for the steel sample. For the diamond tip a Poisson's ratio of 0.07 and a Young's modulus of 1141 GPa was used. The CSM oscillations lead to a multitude of hardness and Young's moduli values during the indentation experiment. Those values were averaged between an indentation depth of 1500 nm and 1900 nm and used to compare different charging conditions.

2.3. Cell design and calibration

2.3.1. Conventional front-side charging approach

The front-side charging cell used for the experiments is depicted in Fig. 1 and a detailed description can be found in an earlier publication [7]. To operate this cell, a tip with an elongated indenter shaft for fluid environments is used to accomplish indentation experiments through the electrolyte. Moreover, the indentation system has to be equipped with a lifting table to adjust the sample position to the designated microscope focus height and indentation height, as well as to allow for the elongated tip to be submerged into the electrolyte. Barnoush and Vehoff used an indentation system with an elongated indenter tip and a mobile measurement head [22] instead of the lifting table. Overall, both the elongated shaft and the lifting table reduce the machine/frame stiffness of the nanoindentation system.

To avoid post-experimental manual adjustment, the tip area function as well as the custom system stiffness was evaluated by mounting a fused silica specimen on top of a dummy sample. During the experiments, the sample is held in place with the Teflon cover and an additional sealing to avoid leakage of the electrolyte compartment. A platinum wire and an Ag/AgCl electrode was used as counter/reference electrode, respectively.

2.3.2. Side charging cell

The novel side charging cell, shown in Fig. 2, was developed to use standard metallographic stub geometry with a diameter of 40 mm, which can be included in a conventional indentation sample tray. This setup offers the further advantage that the cell can be used in any indentation system (as exemplified in Fig. 2b) without the need of an external lifting table, movable measurement head or an elongated tip for fluid environments. Moreover, it can be utilized in an X-ray diffractometer (see Section 2.5) or other devices to perform in situ measurements. The side charging cell consists of a Teflon electrolyte compartment, which holds roughly 8 ml of electrolyte depending on the sample size. An aluminum adapter was used to hold the sample with the geometry of 16 mm × 10 mm × 2 mm in an upright position. The base plate was manufactured of aluminum and connects the adapter piece to the electrolyte compartment. The sample is electrically contacted via the base plate and the adapter piece. A platinum wire is used as counter electrode and the electrolyte is filled up to the conical marking on the Teflon compartment, so that the sample juts out of the electrolyte by 1.0 to 1.5 mm. This jut ensures that the electrolyte does not cover the top sample surface even if bubbles form. Based on this considerations, the maximum diffusion distance to the middle of the sample's top surface is $\approx$ 1.5 mm.

The novel cell design also allows to easily adjust the setup to sheet materials with different thicknesses and it allows to test cylindrical samples by replacing the adapter. Furthermore, the outer cell diameter could be modified to other diameters if necessary.

2.4. Electrochemical parameters

An electrolyte according to [19], consisting of 1.3 mol/l sodium tetraborate decahydrate ($Na_2B_4O_7{\cdot}10H_2O$) in glycerol ($(HOCH_2)_2$-CHOH) was used to decrease the amount of surface damage introduced during front-side charging. The solution was diluted with 20 vol% distilled water to reach adequate conductivity. 1 g/l thiourea (CH_4N_2S) was added as recombination poison to enhance hydrogen adsorption. The sample was connected as the cathode and a platinum wire was used as anode. The exposed cathode surface was assumed to be 1.33 cm^2 for the front-side charging and 3 cm^2 for the side charging setup. A *Gamry 1010B potentiostat (Gamry Instruments, USA)* was used for all ECNI and in situ XRD experiments. Indentations were performed (*i*) without electrolyte, (*ii*) after adding electrolyte while leaving the cell under open circuit potential (OCP), (*iii*) after charging the sample with 1, 2 and 3 mA/cm^2 and (*iv*) after a holding period of 100 h in air. For both cell designs, the current density was kept constant during the indentations to enable a continuous hydrogen supply and comparable results. To ensure that the hydrogen has sufficient time to diffuse to the indent location during side charging, each charging step was performed for 3 h before the indentations started. The duration was decreased to 1 h for the front-side charging cell, since the hydrogen is formed directly at the indent site. A diffusion coefficient of $1.5 \cdot 10^{-6}$ cm^2/s, similar to [4], was assumed.

2.5. In situ XRD

Confirming the presence of hydrogen originating from

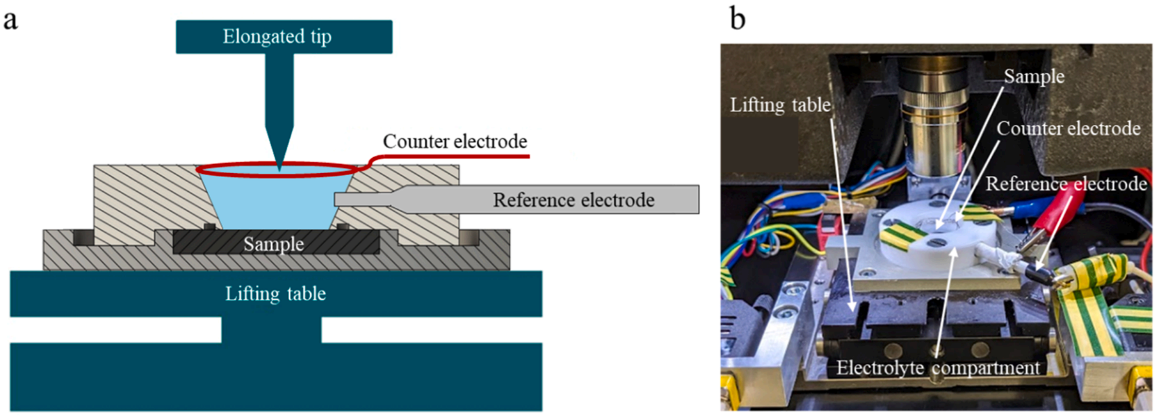

Fig. 1. (a) Schematic drawing (adapted from Ebner et al. [7]) and (b) photograph of the front-side charging cell. The sample in (a) is depicted as a black rectangle.

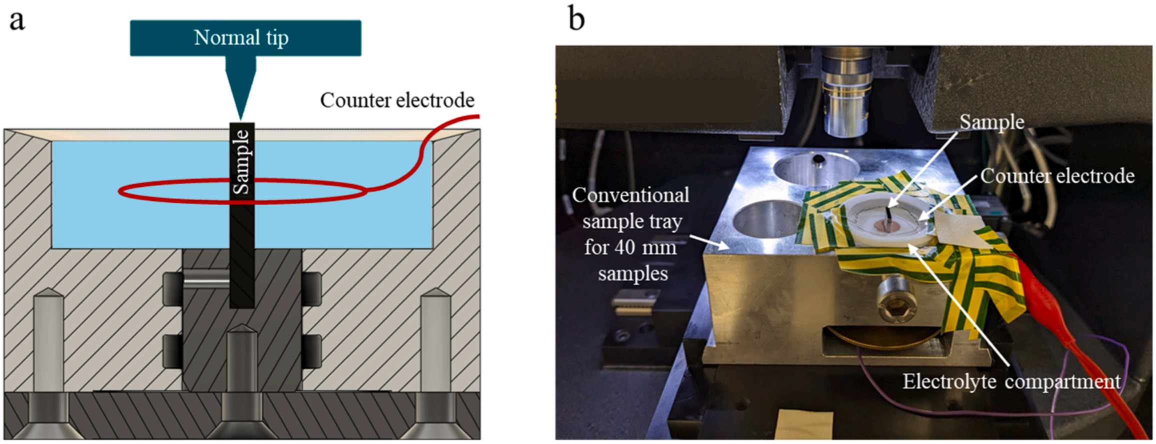

Fig. 2. (a) Schematic drawing of the novel side charging setup. The sample is depicted as a black rectangle. (b) Photograph of the novel side charging setup in a conventional sample tray for 40 mm samples.

electrochemical charging presents a consistent challenge in the hydrogen embrittlement and ECNI community. To address this question, in situ XRD measurements were employed. Accordingly, the side charging cell, as depicted in Fig. 2a, was placed in an adapter and mounted in a *Bruker-AXS D8 Advance diffractometer (Bruker, Germany)* (see Fig. S 1). The measurements were conducted in Bragg-Brentano geometry utilizing CuK_α radiation. Diffractograms were acquired within the 2θ range from 30° to 90° with a step size of 0.01° and an integration time of 0.5 s. Measurements were performed on the Ti-coated sample before the charging process started and were repeated every 3 h after the charging started, up to a maximum duration of 21 h. Initially, a current density of 1 mA/cm^2 was applied for the first 6 h of charging. Afterwards, the current density was increased to 3 mA/cm^2 for the subsequent 15 h to ensure a sufficient hydrogen supply.

3. Results and discussion

3.1. Microstructure

As depicted in Fig. 3a and b, due to the heat treatment, grain sizes above 1 mm were observed for the side charged and front-side charged sample, respectively. Both samples were scanned via EBSD to find similarly oriented grains. The angular deviation of the tested grains, which are highlighted in Fig. 3a and b by bold lines, from an ideal (1 0 1) grain was evaluated via inverse pole figures. In case of the side and front-side charged sample, an angular deviation of ≈ 7° and ≈ 10° was found, respectively; while those grains showed a deviation of ≈ 6° between each other. These small deviations enable to directly compare the indentation results. Indents on and close to grain boundaries and in other grains were not considered in the evaluation. The Vickers micro-indents visible in Fig. 3a and b were used as markers to navigate during the indentation experiments.

3.2. In situ XRD

The applied measurement principle assumes, that hydrogen is absorbed into the steel sample and diffuses to the top surface where it interacts with the Ti film. Fig. 4 presents diffractograms obtained before and during hydrogen charging of the Ti-coated steel sample. The global scan in Fig. 4a shows a high-intensity peak originating from the Ti film, at a diffraction angle of ≈ 38.4°, both before and after 21 h of hydrogen charging. Peaks from the ferritic substrate material appear at higher diffraction angles of ≈ 64.8° and ≈ 82.1°, also visible both before and after 21 h of hydrogen charging. The deviation from the position to the depicted value from the database is assumed to originate from the high chromium content and other alloying elements in the ferritic steel. The higher intensity of the two ferrite peaks before charging in comparison to during the charging is a consequence of a slightly different sample position. The measurement before charging was conducted prior to the mounting of the wires used for the electrochemical charging. Additionally, the measurement after 21 h of charging shows a significant peak evolved at a diffraction angle of ≈ 35.2°, matching the expected peak positions for titanium hydrides. A detailed observation of the peak position during hydrogen charging in Fig. 4b shows a steady shift of the Ti peak to lower diffraction angles. This observation can be related to interstitial hydrogen increasing the lattice constant of Ti and therefore

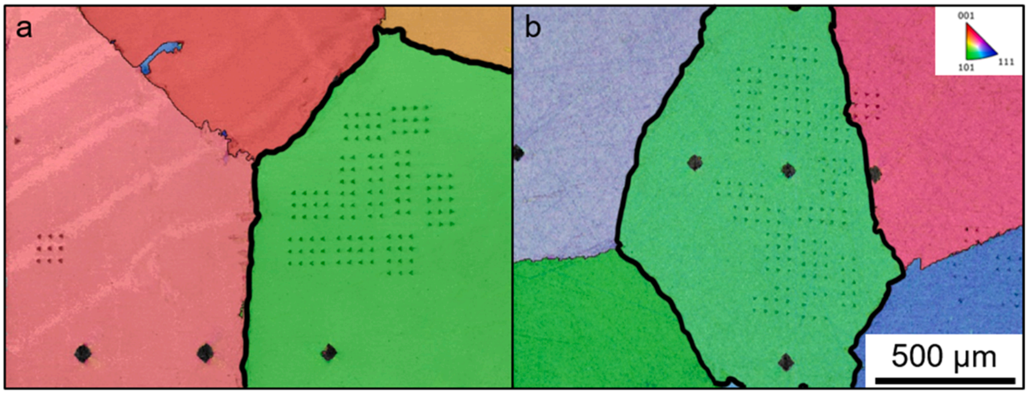

Fig. 3. EBSD inverse pole figure maps of the (a) side charged and (b) front-side charged sample. The grain, which was tested shows an orientation close to (1 0 1) and is highlighted with bold lines. The Vickers microindents were used for navigation during the indentation experiments.

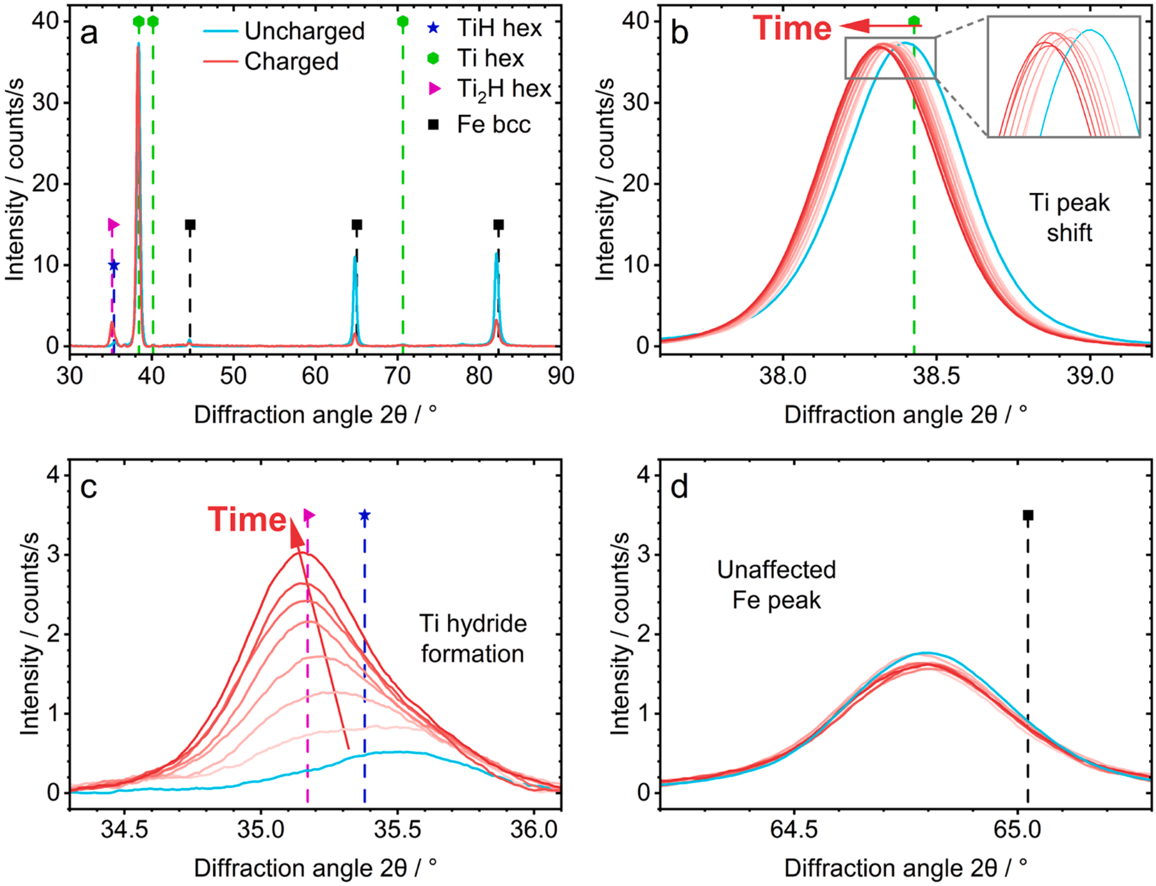

Fig. 4. X-ray diffractograms of the Ti-coated steel sample. (a) Global scan before charging (cyan) and after 21 h of charging (dark red). Peaks before charging (cyan) and evolution during hydrogen charging from 3 h to 21 h (light red to dark red) for (b) Ti peak, (c) titanium hydride peaks and (d) steel/iron substrate peak. Note that the intensity of the peak before charging (cyan) in (d) was adapted for an easier comparison of the peak position.

shifting the peak to lower diffraction angles, consistent with observations made by Pogrielz et al. [27] for the austenitic phase of a duplex steel during hydrogen charging. However, it needs to be noted that possible effects occurring at the interface between steel and Ti could lead to a change of the residual stresses in the Ti film, which would also result in a change of the peak position. Therefore, the formation of the titanium hydride peak in Fig. 4c is a more obvious proof, that hydrogen is present in the self-reporting Ti film and therefore in the underlying steel substrate. The intensity of the titanium hydride peak increases with charging time, representing a self-evident consequence of the ongoing hydrogen supply. Furthermore, the slight asymmetrical peak and the shift to lower diffraction angles over charging time indicates that more than one titanium hydride phases are formed. Fig. 4d shows that the peak position of the ferritic steel substrate is unaffected by hydrogen charging, consistent with the results observed by Pogrielz et al. [27] for ferrite. Preliminary results during this work also showed that no differences in the diffractograms were present when a sample without Ti as a self-reporting film was charged.

3.3. Indentation

Fig. 5a and b present exemplary load-displacement curves for the different tested hydrogen charging conditions on the side and front-side charged sample, respectively. In general, the depth-controlled curves in both graphs exhibit a similar shape, with higher maximum loads reached for the experiments performed during electrochemical charging compared to those obtained before and after charging. Since the overall frame stiffness differs from that for conventional measurements without ECNI for both setups, the frame stiffness is adjusted post-deformation by assuming a depth independent Young's modulus. Therefore, the detailed post-deformation adjustment of the frame stiffness and thus evaluation of Young's modulus yields constant values over the indentation depth for the side charged (Fig. 5c) and front-side charged (Fig. 5d) sample. As a further result, the total system stiffness can be evaluated, indicating a stiffness increase by ≈ 60 % from $2.1 \cdot 10^6$ N/m for the front-side charging cell to $3.4 \cdot 10^6$ N/m for the side charging cell. The hardness values for the side charged and front-side charged sample are depicted in Fig. 5e and f, in which a hardness increase is seen in both cases for the indentation experiments during charging.

The average Young's modulus and hardness values between 1500 nm and 1900 nm from all indents are summarized in Fig. 6. Fig. 6a and b depict Young's moduli, which show no significant variation before, during and after charging for the respective cell types. Furthermore, a comparison of Young's moduli obtained during side charging and front-side charging (Fig. 6a and b) shows no significant difference. The hardness evolution of the side charged sample is presented in Fig. 6c and shows constant hardness values before adding electrolyte to the cell ("inAir") and after adding electrolyte without applying any external voltage ("OCP"). Note that in the case of the side charging approach, the tested surface was continuously exposed to air. During applying an external voltage, a stepwise hardness increase was measured while higher current densities resulted in higher hardness values. This hardness increase can be explained by an increasing hydrogen content in the sample, which leads to higher pinning forces due to hydrogen Cottrell atmospheres near dislocation cores [32]. Thus, a maximal hardness increase of 15 % was measured for the side charged sample. 100 h after the charging procedure, the dissolved hydrogen is assumed to be diffused out of the material and consequently the original hardness values were

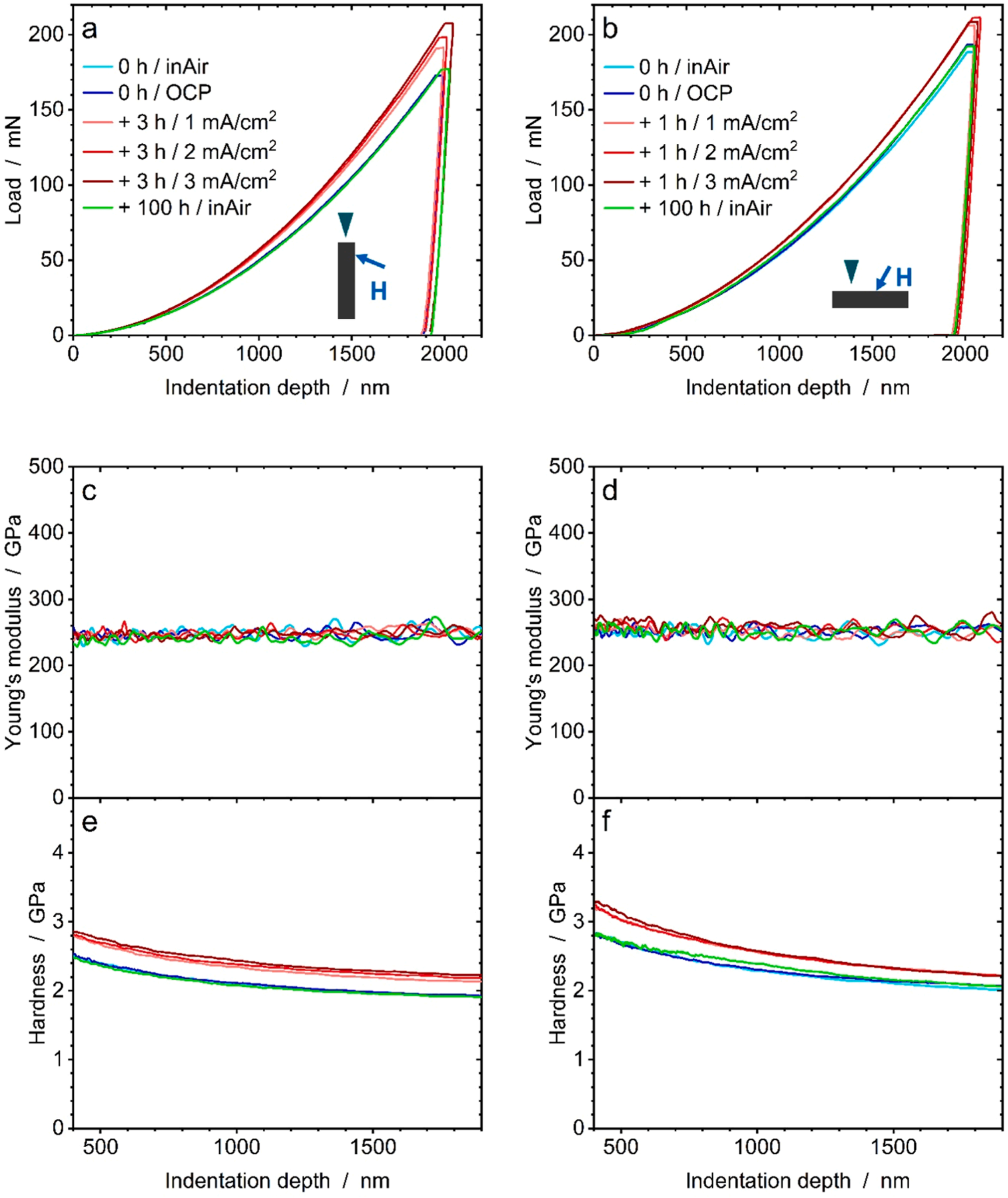

Fig. 5. (a, b) Load–displacement diagrams and (c, d) Young's modulus as well as (e, f) hardness over indentation depth for side charging on the left hand side (a, c, e) and front-side charging on the right hand side (b, d, f). All diagrams contain exemplary curves for the indentation experiments before charging (cyan and blue), during charging (light red to dark red) and 100 h after charging (green). Note that the cyan, blue and green curves overlap. The insets in (a) and (b) show the indentation direction by a dark green triangle and the hydrogen charging with a H.

measured again. A similar hardness evolution was observed for the front-side charged sample in Fig. 6d with slightly higher scattering and a maximal hardness increase of 10 %. More data scattering for the measurements during charging can be explained by bubble formation on the sample-electrolyte interface and the testing through the electrolyte, which correspondingly leads to more instabilities during the measurements; a disadvantage which can be avoided by the novel side charging approach.

Generally, the constant Young's moduli and the hardness increase and decrease during ECNI are in accordance with the back-side charging results reported in [3,4], where several Fe-Cr alloys with 16 to 21 at.% Cr have been investigated. However, Duarte et al. [4] observed a decreasing Young's modulus and hardness during front-side charging. It is assumed that the reason for the change in Young's modulus in [4] could be the evaluation of Young's modulus in a rather low depth of 90 to 100 nm, where the electrolyte might influence the results. According to the data sheet of the X6Cr17 steel, the uniaxial Young's modulus of a polycrystalline sample is 220 GPa at 20 °C [33]. Pure iron shows a Young's modulus of 208.2 GPa in the polycrystalline condition, while a single crystalline grain with a (1 1 0) orientation shows slightly higher values of 214.3 GPa [34]. Using this analogy, slightly higher values than 220 GPa are expected for the present measurements on a grain, which is

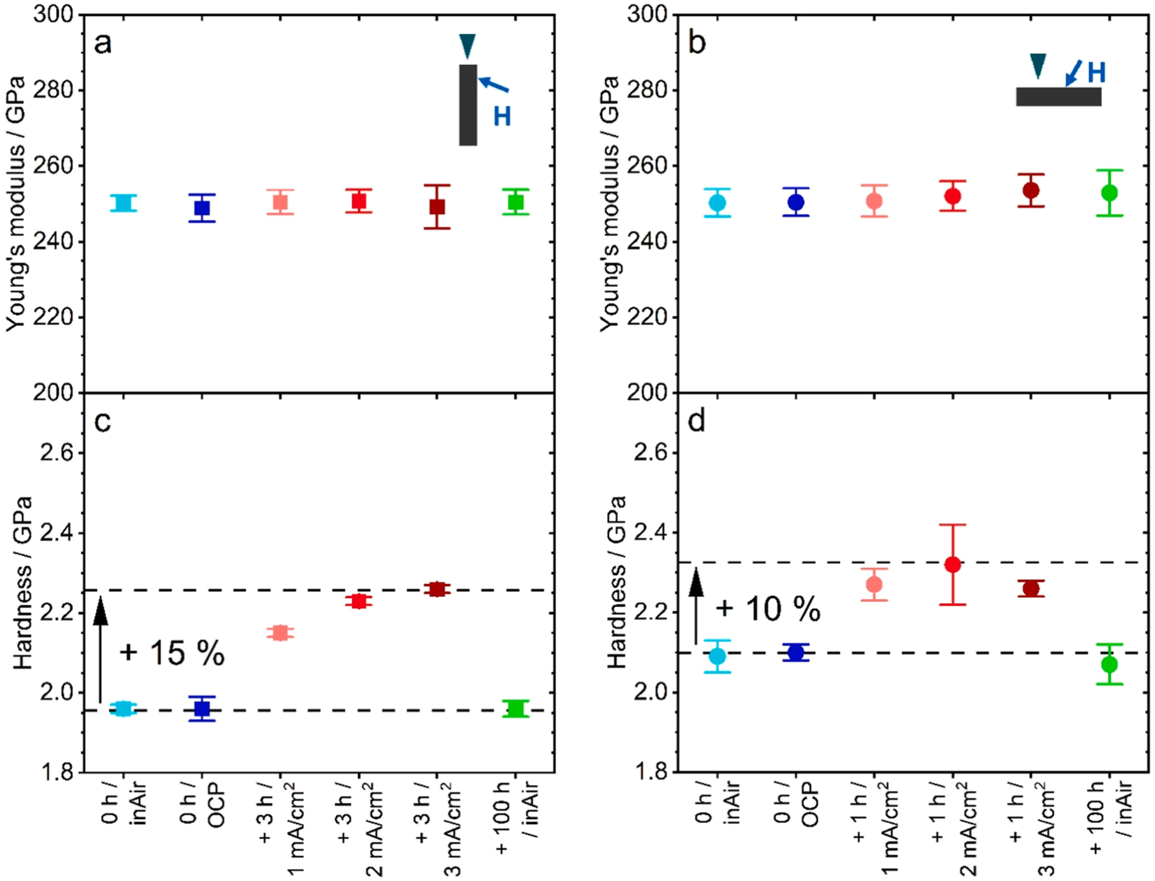

Fig. 6. Averaged values in a depth between 1500 nm and 2000 nm for (a, b) Young's modulus and (c, d) hardness from all performed indentation experiments. The results for side charging are depicted on the left hand side (a, c) and the front-side charging on the right hand side (b, d). All diagrams contain information about the indents before charging (cyan and blue), during charging (light red to dark red) and 100 h after charging (green). The insets in (a) and (b) show the indentation direction by a dark green triangle and the hydrogen charging with a H.

close to a (1 0 1) surface plane orientation. Furthermore, the Oliver and Pharr evaluation [31] typically leads to an overestimation of the Young's modulus and hardness when pile-ups form during the experiment. Those pile-ups are depicted in Fig. 7a and b for the side charged and front-side charged sample, respectively. No significant difference in the pile-up behavior at indents before and during charging are observed when comparing the different charging approaches. Therefore, no pile-up correction was applied to either set of results.

The lower initial hardness during side charging compared to the front-side charged sample can be explained by a lower dislocation density due to an improved surface preparation. Another indicator for a better surface quality is the appearance of pop-ins for the side charged sample, which only appear at low dislocation densities and are not observed for the front-side charged sample (see Fig. S 2). Furthermore,

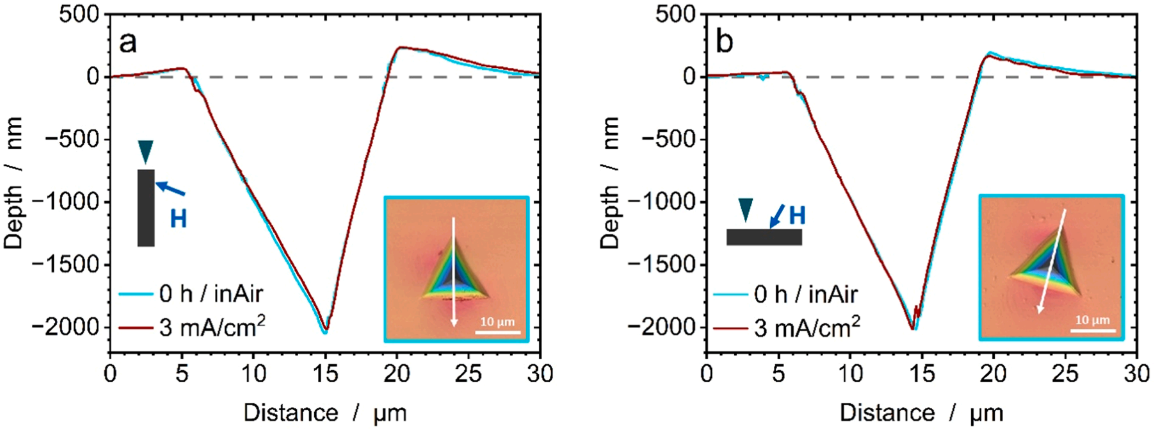

Fig. 7. Comparison of the pile-up formation of the (a) side charged sample and (b) front-side charged sample. The laser confocal microscopy pictures show indents in the uncharged condition (0 h / inAir) (cyan). The arrow indicates the direction for the profile measurements. The same direction was chosen for the profile measurements of the indent in the charged condition (3 mA/cm^2) (dark red). The insets in (a) and (b) show the indentation direction by a dark green triangle and the hydrogen charging with a H.

those pop-ins were detected at lower loads for the charged condition as shown in Fig. S 3. Duarte et al. made comparable observations in a similar alloy [4]. It can be excluded, that the lower system stiffness of the front-side charging cell and the applied stiffness correction falsify the hardness evaluation, as the same sample was also tested on a standard cylindrical sample holder (see Fig. S 2b and section “Influence of the system stiffness” in the Supporting Information). When comparing side and front-side charging, differences in the local Cr content can be excluded after comparing the samples by energy-dispersive X-ray spectroscopy (EDX). The lower hardness during side charging also lead to increased material flow and therefore a more pronounced pile-up formation compared to the front-side charged sample, as visible in Fig. 7a and b.

The novel side charging approach introduces the capability to conduct indentation experiments at various distances from the sample edge. In the experiments outlined in this study, there was minimal variation in distances, particularly for the indentations performed during charging with current densities of 1, 2, and 3 mA/cm^2. Additionally, these experiments aimed to assess the equilibrium condition, which is presumed to be achieved after 3 h of charging at a certain current density, based on the diffusion constant reported by Duarte et al. [4]. The remarkably consistent hardness observed in the subsequent experiments at a certain current density indicates successful attainment of an equilibrium in the tested region (see low standard deviation in Fig. 6c). It is important to note that an increase in the distance from the sample edge necessitates a longer duration to reach equilibrium. Moreover, the equilibrium hydrogen content is anticipated to vary with the distance to the sample edge.

4. Conclusions

We successfully implemented a novel approach for electrochemical nanoindentation and used it to study the changes in mechanical properties of ferritic steel sheets with high chromium content (X6Cr17) due to hydrogen charging. We compared the obtained results with experiments performed with an established front-side hydrogen charging cell. The results for both cell types showed constant Young’s moduli before, during and after charging, while the hardness increased during charging with increasing current densities. The following list summarizes the advantages of the new side charging approach compared to the conventional front-side charging:

- The electrolyte is not in contact with the tested surface and therefore corrosion can be excluded to influence the derived mechanical properties.
- Conventional indenter tips can be used instead of tips with elongated shafts for fluid environments.
- Bubble formation at the electrolyte-sample interface is not directly influencing the measurements because it takes place elsewhere from the indent site – this leads to less instabilities and scattering during the measurements.
- The total system stiffness is increased by ≈ 60 % compared to the reference front-side charging cell [7], while it is expected that a further stiffness improvement occurs when changing from a sheet geometry to a cylinder geometry, because the sheet adapter adds additional compliance.
- The cell can also be employed in other devices, such as an X-ray diffractometer, to perform in situ measurements.

This list mostly applies to bcc materials, which possess a high hydrogen diffusion constant. However, when investigating fcc materials with lower diffusion constants, side charging leads to increased charging times due to a significantly longer diffusion paths.

Besides the disadvantage for metals with a low diffusion constant, the novel side charging approach opens possibilities to investigate hardness differences on the top surface caused by diffusion gradients. Furthermore, the increased stiffness and the versatile sample geometry allow micromechanical experiments such as pillar compressions and bending tests.

Declaration of generative AI and AI-assisted technologies in the writing process

During the preparation of this work the author(s) used “ChatGPT 3.5″ in order to improve readability and language. After using this tool/service, the author(s) reviewed and edited the content as needed and take(s) full responsibility for the content of the publication.

CRediT authorship contribution statement

Stefan Zeiler: Conceptualization, Methodology, Validation, Formal analysis, Investigation, Data curation, Writing – original draft, Writing – review & editing, Visualization, Project administration. **Anna Sophie Jelinek:** Conceptualization, Methodology, Writing – review & editing, Supervision. **Velislava Terziyska:** Resources. **Ruth Schwaiger:** Writing – review & editing, Funding acquisition. **Christian Mitterer:** Writing – review & editing, Supervision, Funding acquisition. **Steffen Brinckmann:** Conceptualization, Writing – review & editing. **Verena Maier-Kiener:** Conceptualization, Methodology, Writing – review & editing, Supervision, Project administration, Funding acquisition.

Declaration of competing interest

The authors declare that they have no known competing financial interests or personal relationships that could have appeared to influence the work reported in this paper.

Acknowledgements

A. S. Jelinek and V. Maier-Kiener acknowledge funding by FFG within the Project PreHy (41901732) carried out in the frame of the program production of the future (“Produktion der Zukunft”) as well as V. Maier-Kiener and C. Mitterer acknowledge funding by the FFG within the Comet-Project Hylley (912671). Moreover, the authors thank Gerhard Hawranek for performing EBSD mapping and are grateful to Daniel Schrittwieser and Nikolaus Kostwein for their assistance during the evaluation of the EBSD maps.

Supplementary materials

Supplementary material associated with this article can be found, in the online version, at doi:10.1016/j.actamat.2024.120113.

References

[1] K.T. Møller, T.R. Jensen, E. Akiba, H. Li, Hydrogen - a sustainable energy carrier, Progress Natural Sci.: Mater. Int. 27 (2017) 34–40, https://doi.org/10.1016/j.pnsc.2016.12.014.

[2] United Nations Framework Convention on Climate Change (UNFCCC), The Paris Agreement, 2016.

[3] J. Rao, S. Lee, G. Dehm, M.J. Duarte, Hardening effect of diffusible hydrogen on bcc Fe-based model alloys by *in situ* backside hydrogen charging, Mater. Des. 232 (2023) 112143, https://doi.org/10.1016/j.matdes.2023.112143.

[4] M.J. Duarte, X. Fang, J. Rao, W. Krieger, S. Brinckmann, G. Dehm, *In situ* nanoindentation during electrochemical hydrogen charging: a comparison between front-side and a novel back-side charging approach, J. Mater. Sci. 56 (2021) 8732–8744, https://doi.org/10.1007/s10853-020-05749-2.

[5] H. Khanchandani, S. Zeiler, L. Strobel, M. Göken, P. Felfer, A carbon stabilized austenitic steel with lower hydrogen embrittlement susceptibility, Steel. Res. Int. (2023) 202300372, https://doi.org/10.1002/srin.202300372.

[6] C. Müller, M. Zamanzade, C. Motz, The impact of hydrogen on mechanical properties; a new *in situ* nanoindentation testing method, Micromachines. (Basel) 10 (2019) 114, https://doi.org/10.3390/mi10020114.

[7] A.S. Ebner, S. Brinckmann, E. Plesiutschnig, H. Clemens, R. Pippan, V. Maier-Kiener, A modified electrochemical nanoindentation setup for probing hydrogen-material interaction demonstrated on a nickel-based alloy, J. Minerals, Metals

Mater. Society 72 (2020) 2020–2029, https://doi.org/10.1007/s11837-020-04104-9.

[8] A.S. Ebner, E. Plesiutschnig, H. Clemens, R. Pippan, V. Maier-Kiener, Rate-depending plastic deformation behaviour in a nickel-base alloy under hydrogen influence, Int. J. Hydrogen. Energy 46 (2021) 38132–38143, https://doi.org/10.1016/j.ijhydene.2021.09.030.

[9] J. Kim, D. Hall, H. Yan, Y. Shi, S. Joseph, S. Fearn, R.J. Chater, D. Dye, C.C. Tasan, Roughening improves hydrogen embrittlement resistance of Ti-6Al-4V, Acta Mater. 220 (2021) 117304, https://doi.org/10.1016/j.actamat.2021.117304.

[10] J. Kim, C.C. Tasan, Microstructural and micro-mechanical characterization during hydrogen charging: an in situ scanning electron microscopy study, Int. J. Hydrogen. Energy 44 (2019) 6333–6343, https://doi.org/10.1016/j.ijhydene.2018.10.128.

[11] A. Barnoush, H. Vehoff, Recent developments in the study of hydrogen embrittlement: hydrogen effect on dislocation nucleation, Acta Mater. 58 (2010) 5274–5285, https://doi.org/10.1016/j.actamat.2010.05.057.

[12] A. Massone, D. Kiener, Prospects of enhancing the understanding of material-hydrogen interaction by novel *in-situ* and in-operando methods, Int. J. Hydrogen. Energy 47 (2022) 10097–10111, https://doi.org/10.1016/j.ijhydene.2022.01.089.

[13] M. Truschner, A. Trautmann, G. Mori, The basics of hydrogen uptake in iron and steel, Berg Huettenmaenn Monatsh 166 (2021) 443–449, https://doi.org/10.1007/s00501-021-01142-x.

[14] D. Wan, Y. Deng, A. Barnoush, Hydrogen embrittlement effect observed by in-situ hydrogen plasma charging on a ferritic alloy, Scr. Mater. 151 (2018) 24–27, https://doi.org/10.1016/j.scriptamat.2018.03.038.

[15] A. Massone, A. Manhard, W. Jacob, A. Drexler, W. Ecker, A. Hohenwarter, S. Wurster, D. Kiener, An SEM compatible plasma cell for in situ studies of hydrogen-material interaction, Rev. Sci. Instr. 91 (2020) 043705, https://doi.org/10.1063/1.5142043.

[16] T. Neeraj, R. Srinivasan, J. Li, Hydrogen embrittlement of ferritic steels: observations on deformation microstructure, nanoscale dimples and failure by nanovoiding, Acta Mater. 60 (2012) 5160–5171, https://doi.org/10.1016/j.actamat.2012.06.014.

[17] A. Barnoush, M. Asgari, R. Johnsen, Resolving the hydrogen effect on dislocation nucleation and mobility by electrochemical nanoindentation, Scr. Mater. 66 (2012) 414–417, https://doi.org/10.1016/j.scriptamat.2011.12.004.

[18] T. Hajilou, Y. Deng, B.R. Rogne, N. Kheradmand, A. Barnoush, In situ electrochemical microcantilever bending test: a new insight into hydrogen enhanced cracking, Scr. Mater. 132 (2017) 17–21, https://doi.org/10.1016/j.scriptamat.2017.01.019.

[19] T. Hajilou, M.S.B. Hope, A.H. Zavieh, N. Kheradmand, R. Johnsen, A. Barnoush, In situ small-scale hydrogen embrittlement testing made easy: an electrolyte for preserving surface integrity at nano-scale during hydrogen charging, Int. J. Hydrogen. Energy 43 (2018) 12516–12529, https://doi.org/10.1016/j.ijhydene.2018.04.168.

[20] Y. Deng, T. Hajilou, D. Wan, N. Kheradmand, A. Barnoush, In-situ micro-cantilever bending test in environmental scanning electron microscope: real time observation of hydrogen enhanced cracking, Scr. Mater. 127 (2017) 19–23, https://doi.org/10.1016/j.scriptamat.2016.08.026.

[21] Y. Deng, A. Barnoush, Hydrogen embrittlement revealed via novel in situ fracture experiments using notched micro-cantilever specimens, Acta Mater. 142 (2018) 236–247, https://doi.org/10.1016/j.actamat.2017.09.057.

[22] A. Barnoush, H. Vehoff, Electrochemical nanoindentation: a new approach to probe hydrogen/deformation interaction, Scr. Mater. 55 (2006) 195–198, https://doi.org/10.1016/j.scriptamat.2006.03.041.

[23] A. Barnoush, H. Vehoff, In situ electrochemical nanoindentation: a technique for local examination of hydrogen embrittlement, Corros. Sci. 50 (2008) 259–267, https://doi.org/10.1016/j.corsci.2007.05.026.

[24] A. Barnoush, H. Vehoff, Hydrogen embrittlement of aluminum in aqueous environments examined by in situ electrochemical nanoindentation, Scr. Mater. 58 (2008) 747–750, https://doi.org/10.1016/j.scriptamat.2007.12.019.

[25] A. Barnoush, C. Bies, H. Vehoff, In situ electrochemical nanoindentation of FeAl (100) single crystal: hydrogen effect on dislocation nucleation, J. Mater. Res. 24 (2009) 1105–1113, https://doi.org/10.1557/jmr.2009.0084.

[26] M. Koyama, D. Yamasaki, T. Nagashima, C.C. Tasan, K. Tsuzaki, In situ observations of silver-decoration evolution under hydrogen permeation: effects of grain boundary misorientation on hydrogen flux in pure iron, Scr. Mater. 129 (2017) 48–51, https://doi.org/10.1016/j.scriptamat.2016.10.027.

[27] T. Pogrielz, M. Eichinger, A. Weiser, J. Todt, A. Hohenwarter, A. Ascii, B. Sarac, D. Brandl, G. Ressel, M. Jary, A. Dlouhy, G. Mori, J. Keckes, Peculiarity of hydrogen absorption in duplex steels: phase-selective lattice swelling and stress evolution, Scr. Mater. 248 (2024) 116142, https://doi.org/10.1016/j.scriptamat.2024.116142.

[28] K. Hirata, S. Iikubo, M. Koyama, K. Tsuzaki, H. Ohtani, First-principles study on hydrogen diffusivity in bcc, fcc and hcp iron, Metall. Mater. Trans. A 49 (2018) 5015–5022, https://doi.org/10.1007/s11661-018-4815-9.

[29] G.P.M. Leyson, B. Grabowski, J. Neugebauer, Multiscale modeling of hydrogen enhanced homogeneous dislocation nucleation, Acta Mater. 107 (2016) 144–151, https://doi.org/10.1016/j.actamat.2016.01.036.

[30] X. Fang, A. Kreter, M. Rasinski, C. Kirchlechner, S. Brinckmann, C. Linsmeier, G. Dehm, Hydrogen embrittlement of tungsten induced by deuterium plasma: insights from nanoindentation tests, J. Mater. Res. 33 (2018) 3530–3536, https://doi.org/10.1557/jmr.2018.305.

[31] W.C. Oliver, G.M. Pharr, An improved technique for determining hardness and elastic modulus using load and displacement sensing indentation experiments, J. Mater. Res. 7 (1992) 1564–1583, https://doi.org/10.1557/JMR.1992.1564.

[32] A.H. Cottrell, M.A. Jaswon, Distribution of solute atoms round a slow dislocation, Proc. Royal Soc. London Series A 199 (1949) 104–114, https://doi.org/10.1098/rspa.1949.0128.

[33] Team Edelstahl, Datasheet X6Cr17, 2023. https://www.teamedelstahl.de/wp-content/uploads/2021/04/1.4016.pdf (accessed December 21, 2023).

[34] S. Takaki, T. Masumura, T. Tsuchiyama, Young's modulus of single crystalline iron and elastic stiffness, Tetsu-to-Hagane 106 (2020) 679–682, https://doi.org/10.2355/tetsutohagane.TETSU-2019-129.